AIAA Journal
Vol. 49, No. 2, February 2011

Quenching of a Boundary-Layer Laminar Diffusion Flame in Microgravity

Hui Ying Wang* and Juan Luis Florenciano Merino*
Institut Pprime, 86961 Futuroscope Chasseneuil Cedex. France

DOI: 10.2514/1.J050640

Radiative quenching of a nonpremixed, heavily sooting, laminar flame established in a shear boundary layer at very low strain rates in microgravity is investigated. The computations include detailed chemistry, transport, and radiation for a three-dimensional reacting flow. Radiative quenching is expected at long residence times, due to soot formation resulting from flame expansion downstream of the flame leading edge. The soot model is based on the formation of two- and three-ringed aromatic species and correctly reproduces the experimental data from a laminar ethylene diffusion flame over a flat plate. The purpose of this study is to better understand the effects of a dimensionless volume coefficient, defined as $C_q = V_F/V_{\mathrm{ox}}$ (where V_F is the fuel-injection velocity and V_{ox} is the airstream velocity), on flame quenching and its standoff in a shear reactive boundary layer. Experiments have shown that a blue unstable flame (negligible radiative feedback) may change to a yellow shorter flame (significant radiative feedback) with an increase of C_q. This experimental trend is numerically reproduced, showing that an increase of C_q results in a reduction in flame length that is significantly affected by increasing V_F or decreasing V_{ox}, favoring soot formation. The flame quenching at very low strain rates is a combination of radiative heat loss and combustion efficiency, depending on the fuel-zone geometry and oxygen concentration. Along a semifinite fuel zone, the ratio d_f/d_b between the flame standoff distance d_f and the boundary-layer thickness d_b converges toward a constant value of 1.2. With reduction in fuel size, radiation loss causes the flame temperature and magnitude of the ratio d_f/d_b to decrease until the flame migrates toward the boundary layer ($d_f/d_b < 1$) far away from the trailing edge. In all cases, the soot resides within the boundary layer far from the flame, despite the fuel-zone size and oxygen concentration. The two-dimensional flow structure is approximate for C_q below 0.02, beyond which the three-dimensional effects are of importance, and the reactive boundary layer is significantly lifted above the surface. This flame behavior cannot be described by the available asymptotical solution from a reactive boundary-layer model without taking into account radiation loss.

Nomenclature

A = preexponential factor
C_q = dimensionless volume coefficient
c_2 = scaling factor in the soot model, $127 \times 10^{8.88}$
c_3 = scaling factor in the soot model, $178 \times 10^{9.50}$
c_4 = scaling factor in the soot model, $9000.6\ \mathrm{kg \cdot m \cdot kmol^{-1} \cdot s^{-1}}$
c_5 = scaling factor in the soot model, $105.81\ \mathrm{kg \cdot m \cdot kmol^{-1} \cdot K^{-1/2} \cdot s^{-1}}$
c_6 = scaling factor in the soot model, $18{,}903.51\ \mathrm{kg \cdot m \cdot kmol^{-1} \cdot K^{-1/2} \cdot s^{-1}}$
D = diffusivity of a mixture, $\mathrm{m^2 \cdot s^{-1}}$
$\bar{D}_a$ = Damköhler number
D_i = diffusivity of species, $\mathrm{m^2 \cdot s^{-1}}$
E = activation energy, K
F_{soot} = integrated soot volume fraction
f_{soot} = soot volume fraction
Gr_x = Grashof number
H_c = heat release rate per unit mass of fuel consumed, $\mathrm{kJ \cdot kg^{-1}}$
H_o = heat release rate per unit mass of oxygen consumed, $13{,}100\ \mathrm{kJ \cdot kg^{-1}}$
h = enthalpy, $\mathrm{J \cdot kg^{-1}}$
I = radiative intensity, $\mathrm{W \cdot m^{-2} \cdot Sr^{-1} \cdot \mu m^{-1}}$
I^l = radiative intensity for a single ordinate direction, l, $\mathrm{W \cdot m^{-2} \cdot Sr^{-1} \cdot \mu m^{-1}}$
k = thermal conductivity, $\mathrm{W \cdot m^{-1} \cdot K^{-1}}$
L_f = length of visible flame, m
L_p = length of the burner, m
M = soot mass density, $\mathrm{kg \cdot m^{-3}}$
M_p = molar mass of a soot nucleus, $12{,}011\ \mathrm{kg \cdot kmol^{-1}}$
$\vec{n}$ = normal direction
$\dot{m}_s''$ = local burning rate per unit area, $\mathrm{kg \cdot m^{-2} \cdot s^{-1}}$
N = soot number density, $\mathrm{particles \cdot m^{-3}}$
N_A = Avogadro's number, $6.022 \times 10^{26}\ \mathrm{kmol^{-1}}$
Pr = Prandtl number
p = pressure, Pa
q_r = radiant energy flux, $\mathrm{W \cdot m^{-2}}$
$\dot{q}''$ = heat release rate per unit volume, $\mathrm{W \cdot m^{-3}}$
Q = calculated heat release rate, kW
Q_R = radiative heat loss rate, kW
Q_T = theoretical heat release rate, kW
R = universal gas constant
Re_x = Reynolds number
S = stoichiometric air-to-fuel ratio by mass
Sc = Schmidt number
T = temperature, K or °C
T_f = flame temperature, K or °C
t = time, s
u = velocity, $\mathrm{m \cdot s^{-1}}$
u_i, u_j = velocity components in the coordinate directions x, y and z, $\mathrm{m \cdot s^{-1}}$
u_i^{th} = thermophoretic velocity components, $\mathrm{m \cdot s^{-1}}$
V_F = fuel-injection velocity, $\mathrm{m \cdot s^{-1}}$
V_{ox} = oxidizer velocity, $\mathrm{m \cdot s^{-1}}$
w^l = weighting factor in the discrete ordinates method
W_p = width of the burner, m
W_f = width of the visible flame, m

Received 31 May 2010; revision received 13 September 2010; accepted for publication 27 September 2010.

*Centre National de la Recherche Scientifique, Unite Propre de Recherche 3346, Département Fluide-Thermique-Combustion, Ecole Nationale Superieure de Mecanique et d'Aerotechnique, B.P. 40109, Téléport 2, 1 Avenue Clément Ader; wang@lcd.ensma.fr.

W_i = molecular weight of species, $\mathrm{kg \cdot kmol^{-1}}$
x = streamwise coordinate
x_i, x_j = coordinate directions x, y, and z
X_F = molar fraction of the fuel
X_{O2} = molar fraction of oxygen
Y_i = mass fraction of species
Y_{O} = oxygen mass fraction
$Y_{\mathrm{O},\infty}$ = oxygen mass fraction of a freestream
y = cross-stream coordinate
Z = mixture fraction
Z_s = mixture fraction at the burner boundary
Z_{st} = stoichiometric ratio of mixture fraction
z = vertical coordinate
α_∞ = freestream thermal diffusivity, $\mathrm{m^2 \cdot s^{-1}}$
δ_f = thickness of the visible flame, m or mm
ε = thickness of the flame sheet, m or mm
κ = total absorption coefficient, $\mathrm{m^{-1}}$
μ = dynamic viscosity, $\mathrm{kg \cdot m^{-1} \cdot s^{-1}}$
ξ = ratio between buoyant forces and inertia
ρ = density, $\mathrm{kg \cdot m^{-3}}$
ρ_{soot} = soot density, $\mathrm{kg \cdot m^{-3}}$
σ = Stefan–Boltzmann constant
τ = soot collision efficiency, 0.13 or characteristic time, s
τ_{ch} = characteristic chemical time, s
τ_{re} = characteristic residence time, s
Ω = solid angle of the radiation propagation, Sr
$\boldsymbol{\Omega}$ = direction of the radiation propagation
$\dot{\omega}_{M,\mathrm{gro}}$ = rate of the soot surface growth, $\mathrm{kg \cdot s^{-1} \cdot m^{-3}}$
$\dot{\omega}_{M,\mathrm{inc}}$ = rate of the soot mass density inception, $\mathrm{kg \cdot s^{-1} \cdot m^{-3}}$
$\dot{\omega}_{M,\mathrm{ox}}$ = soot oxidation rate, $\mathrm{kg \cdot s^{-1} \cdot m^{-3}}$
$\dot{\omega}_{N,\mathrm{coa}}$ = rate of the soot number coagulation, $\mathrm{particles \cdot s^{-1} \cdot m^{-3}}$
$\dot{\omega}_{N,\mathrm{inc}}$ = rate of the soot number inception, $\mathrm{particles \cdot s^{-1} \cdot m^{-3}}$
$\dot{\omega}_{\mathrm{o}}$ = oxygen consumption rate, $\mathrm{kg \cdot s^{-1} \cdot m^{-3}}$

I. Introduction

A FIRE onboard spacecraft (though unlikely, due to strict safety measures) is one of the scenarios with the highest damage potential for hardware and crew. In normal gravity, buoyancy-induced flow may be laminar when the scale is small and transition to turbulence as the size of the fuel increases. Because of the absence of natural convection in spacecraft, the flow is limited to that induced by external forced advection. Characteristic velocities of a heat-ventilation or air-conditioning system in spacecraft are of the order of $0.1\ \mathrm{m/s}$; therefore, the flow is expected to be laminar. The most likely scenario of a flame incidentally initiated and spread onboard spacecraft is a wall of combustible material adjacent to a low-Reynolds-number gas flow (forced by the venting system) and exposed to a critical ignition source. As a major portion of heat released from the igniting stage of combustion is transported by convection in the flow direction, the superior mode of spread is of cocurrent (forward) type. A renewed interest in such fire propagation at very low Reynolds numbers ($Re < 100$) under conditions of reduced gravity in spacecraft has arisen in the past two decades [1]. This type flame can be described by the ratio between buoyant forces and inertia, defined as follows: $\xi = Gr_x / Re_x^{5/2}$, where Re_x is the Reynolds number and Gr_x the Grashof number [2]. The experimental work [2] shows that if the magnitude of the forced flow is small, an almost vertical plume is formed (see Fig. 1a), indicating a predominant natural convection ($\xi > 1$). Under microgravity conditions, the ratio ξ is much lower than unity, and even for a low-Reynolds-number flow ($Re < 100$), a boundary-layer diffusion flame is observed to appear (see Fig. 1b), suggesting a predominant forced convection ($\xi \leq 1$).

In the absence of natural convection, radiation is the predominant mode of heat transfer, even for a small forward diffusion flame [3]. Konsur et al. [4] attempted to describe the sooting behavior of nonbuoyant jet diffusion flame by using the smoke-point concept originally proposed by Markstein and De Ris [5]. Cocurrent flame spread over a solid plate could then be linked to a critical soot concentration [6]. Despite the practical utility of this approach, a proper evaluation of material flammability requires a detailed understanding of the effect of oxidizer flow velocity on the local soot concentrations to which the structure of the flowfield in the vicinity of the flame connects. Several experimental investigations [7,8] have demonstrated how changes in blowing affect the soot formation, and thus the flame structure, in the absence of natural convection. Rouvreau et al. [9] numerically predicted two regimes (attached and detached flows) of a low-Reynolds-number flow in the absence of natural convection, function of blowing, and thermal expansion. The position and value of the peak temperature are accurately predicted by the numerical model. The key trends in the evolution with downstream distance are captured by the computed profiles. However, in the Rouvreau et al. works, thermal radiation is not included, and 40% of energy was subtracted numerically to provide a correct flame temperature. Moreover, most of the work [9,10] concentrated on the description and explanation of velocity overshoots close to the reacting zone.

Diffusion flame quenching is of both fundamental and practical interest to applications such as fire spread over a condensed-fuel surface. Flame extinction can be characterized as either kinetic (i.e., diffusion) or radiative. Kinetic extinction occurs at short residence times (i.e., at high strain rates or scalar dissipation rates) and has been extensively studied in laminar diffusion flames [11], whereas radiative extinction is expected at long residence times and thus

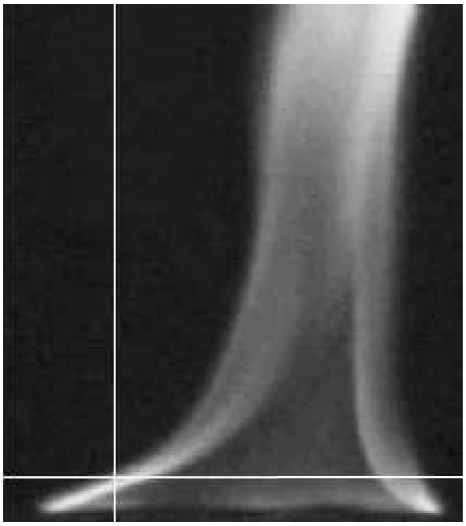

a) Normal gravity

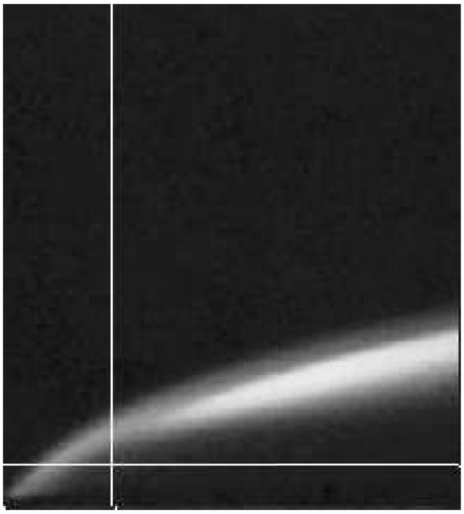

b) Micro gravity

Fig. 1 Structure of nonpremixed reacting flow from experiment.

occurs at very low strain rates. For this reason, it is of particular interest for spacecraft fire safety, when buoyancy is not available to accelerate (strain) the flowfield. Radiative extinction has been reported for gaseous spherical diffusion flames in microgravity [12]. Microgravity experiments [7,8] allowed the first observation of flame quenching for boundary-layer diffusion flame. There is no analytical solution to the problem of blowing in a reacting boundary layer with the consideration of radiative loss [13]. A simple scaling analysis [14] for flame standoff is limited to a reacting flow with uniform density. On the other hand, experimental study at large fuel size creates an insurmountable difficulty under microgravity conditions, due to strict safety measures. A complementary numerical study appears to be necessary.

Quenching of a boundary-layer diffusion flame at very low strain rates is much more difficult to predict, due to radiative loss coupled with complex chemical processes of soot formation, which are not fully understood. Currently, for predicting the local soot concentration, extensive efforts are devoted in 3-D computational fluid dynamics codes to the semi-empirical soot models [15–18] involving the inception, coagulation, surface growth, and oxidation processes. Nonbuoyant laminar jet diffusion flames have been modeled for ethylene/air, by assuming the nucleation and growth of soot are first-order functions of acetylene concentrations [15,16]. Recent research suggests that the growth of aromatics is the rate-limiting step, rather than the formation of the first ring [17]. Vovelle et al. [18] showed that in decane flames, aromatic hydrocarbons are formed from acetylene. Anderson et al. [19] showed that even a small quantity of aromatic hydrocarbons in the fuel can significantly increase the soot emissions. In their study of a laminar methane flame, Hall et al. [20] developed a soot inception rate based on the formation of two- and three-ringed aromatic species from single-ringed aromatic species using a simplified reaction mechanism. However, accuracy of the semi-empirical soot models seems to be strongly linked to the configuration studied, and no guarantees are given that validation applies to a cocurrent boundary-type laminar flame in microgravity. This paper tends to use a polycyclic aromatic hydrocarbon (PAH) inception model for predicting the soot volume fraction on such a flame by employing a detailed kinetic reaction mechanism [21]. A radiation heat transfer model that considered the soot, water, and CO_2 mixture is included. During experiments, microgravity conditions are attained by means of parabolic flights, and the experimental work [8] serves to validate the numerical models. Generally, a good agreement with the measured soot volume fraction is achieved by the PAH inception model. Both prediction and experiment show that soot production is enhanced with decreasing the oxidizer flow velocity or increasing the fuel-injection rate, further emphasizing the role of radiation on the geometric characteristics of a cocurrent boundary-layer laminar flame in microgravity. As a complementary study, the numerical simulation helps to emphasize the impact that the soot formation has on the flame quenching and can be used to investigate the flame propagation at large fuel size.

II. Theoretical Model

Because radiation is inherently a 3-D phenomenon, the Navier–Stokes fluid dynamic equations of three-dimensional elliptic reacting flow are solved.

A. Fluid Dynamic Equations

The hydrodynamic model is based on a classical reactive-flow model.

Mass conservation:

$$\frac{\partial \rho}{\partial t} + \nabla \cdot \rho u = 0 \tag{1}$$

Momentum conservation:

$$\frac{\partial \rho u}{\partial t} + \nabla \cdot \rho u u = -\nabla p + \nabla \cdot \tau_{ij} \tag{2}$$

State equation:

$$p = \rho T \frac{R}{M} \tag{3}$$

Energy conservation:

$$\frac{\partial \rho h}{\partial t} + \nabla \cdot \rho h u = \nabla \cdot k \nabla T + \dot{q}''' - \nabla \cdot q_r \tag{4}$$

In the Shvab–Zel'dovich energy equation (4), h represents the sensible enthalpy. Because the unit Lewis number ($Pr = Sc$) is used, the enthalpy flux from the diffusing species is taken into account through the heat release rate by employing both Fick's law and species conservation. For a laminar flame, diffusivity D_i, thermal conductivity k, and viscosity are approximated from kinetic theory [22], because the temperature dependence of each is important in a reactive system.

B. Combustion Model

The combustion model is based on the assumption that combustion is mixing-controlled. A linear combination of the conservation equation for fuel and oxidizer leads to the following transport equation for the mixture fraction Z, which is a conserved quantity from a normalized mass ratio between fuel and oxidizer:

$$\frac{\partial \rho Z}{\partial t} + \frac{\partial (\rho u_i Z)}{\partial x_j} = \frac{\partial}{\partial x_j}\left(\frac{\mu}{Sc}\frac{\partial Z}{\partial x_j}\right) \tag{5}$$

The oxygen mass conservation equation is given as

$$\frac{\partial \rho Y_{\mathrm{O}}}{\partial t} + \frac{\partial (\rho u_i Y_{\mathrm{O}})}{\partial x_j} = \frac{\partial}{\partial x_j}\left(\frac{\mu}{Sc}\frac{\partial Y_{\mathrm{O}}}{\partial x_j}\right) + \dot{\omega}'''_{\mathrm{O}} \tag{6}$$

Gaseous species diffusivity is inferred from the viscosity ($\rho D = \mu/Sc$), assuming a Schmidt number equal to 0.7. By combining the two conservation equations of the mixture fraction (5) and oxygen mass fraction (6), and after a mathematical arrangement, an expression for the rate of oxygen mass consumption can be derived:

$$-\omega'''_{\mathrm{O}} = \frac{\partial}{\partial x_j}\left(\frac{\mu}{Sc}\frac{\mathrm{d}Y_{\mathrm{O}}}{\mathrm{d}Z}\frac{\partial Z}{\partial x_j}\right) - \frac{\mathrm{d}Y_{\mathrm{O}}}{\mathrm{d}Z}\frac{\partial}{\partial x_j}\left(\frac{\mu}{Sc}\frac{\partial Z}{\partial x_j}\right) = \frac{\mu}{Sc}\frac{\mathrm{d}^2 Y_{\mathrm{O}}}{\mathrm{d}Z^2}|\nabla Z|^2 \tag{7}$$

Neither of the expressions in Eq. (7) for the local oxygen consumption rate is particularly convenient to apply numerically, because of the discontinuity of the derivative of $Y_{\mathrm{O}}(Z)$ at stoichiometric ratio $Z = Z_{\mathrm{st}}$ from the state relation. However, an expression for the oxygen consumption rate in units of mass per unit time per unit area of flame sheet can be derived from Eq. (7):

$$-\omega''_{\mathrm{O}} = \left.\frac{\mathrm{d}Y_{\mathrm{o}}}{\mathrm{d}Z}\right|_{Z<Z\mathrm{st}} \frac{\mu}{Sc}\nabla Z \cdot \mathbf{n} \tag{8}$$

Note that the numerical procedure entails the subdividing of the calculation domain into a finite number of cells. From Eq. (8), the local heat release rate per unit area can computed by locating the flame sheet at the stoichiometric surface. If a grid cell is much larger than the flame-sheet thickness ($\leq$ 1 mm), this energy will be distributed to the grid cells cut by the flame sheet [22]. Because the temperature is smeared out over a grid cell, the computations should be grid-independent by reducing the cell dimensions to a sufficient small value. In such a study, the grid resolution is sufficiently fine (about 1 mm near the reaction zone) to resolve the flame sheet, and the heat release rate is directly proportional to the rate of oxygen consumption [23] at the grid cell, giving a grid-independent resolution:

$$\dot{q}''' = -H_{\mathrm{o}}\omega'''_{\mathrm{O}} \tag{9}$$

In gaseous combustion, the chemical compositions are found by using an appropriate reaction mechanism. For providing the local concentration of soot precursory species, such as acetylene (C_2H_2), benzene (C_6H_6), and phenyl (C_6H_5), a detailed kinetic reaction [21], including 736 reversible reactions and 99 species, has to be used to model the combustion for ethylene/air. This reaction mechanism consists of a set of elementary reactions with corresponding rate parameters. The rate coefficient for reaction is calculated from an Arrhenius expression. These rate parameters, together with the elementary reactions and their stoichiometric coefficients, constitute the reaction mechanism. The rate laws for the species can be calculated by using a time-consuming stiff ordinary-differential-equation solver. However, any attempt to use the Arrhenius expression for a detailed kinetic [21] coupled with a three-dimensional elliptic reacting flow is discouraged, due to the problem of computational cost.

In combustion, the mixture fraction is a conserved quantity traditionally that is defined as the (mass) fraction of the gas mixture that originates in the fuel stream. The mixture fraction is a function of space and time, commonly denoted as $Z(x, t)$. Therefore, many combustion models employ a detailed cost-effective kinetic reaction by tabulating the kinetics in terms of mixture fraction, and only the mixture fraction is tracked in the calculation [24]. This implies that all species of interest of combustion products can be described in terms of the mixture fraction alone. The correspondence between the mass fraction of an individual species and the mixture fraction is called its state relation. This state relation can be obtained by using the OPPDIF (Opposed Diffusion Flames) computer code [25], which is performed by using subroutines from the chemical program library Chemkin.

As an illustration, dependence of the main chemical species on mixture fraction is presented in Fig. 2. For obtaining such a state relation for combustion of fuel/air, OPPDIF [25] requires chemical and physical input parameters, such as the fuel type, the initial temperature value of fuel and oxygen, the initial value of fuel and oxygen mass fraction, pressure, and strain rate. In this study, the chemical-composition profiles for combustion of ethylene/air as a function of the mixture fraction (see Fig. 2) correspond to the temperature ($T_F = T_{\mathrm{OX}} = 300$ K), pressure ($P = 1$ atm), and compositions ($X_{\mathrm{O2}} = 0.21$ and 0.35) found in the experiment [8]. A small value of the strain rate (less than 0.0003) that is much lower than the critical extinction value is assigned, corresponding to the chemical equilibrium conditions. Note that this state relation obtained from OPPDIF [25] is independent of reactant and oxidizer flow rates. At the start of a simulation, the detailed chemical species involved are tabulated as a function of mixture fraction. During the simulation, the local value of all species is found by table lookup according to the local mixture-fraction value.

C. Radiative Heat Transfer

In this laminar flame, soot is the most important combustion product controlling the thermal radiation from the flame. As the radiation spectrum of soot is continuous, it is possible to assume that the gas behaves as a gray medium. The spectral dependence is then lumped into one absorption coefficient κ. The source term is given by the blackbody radiation intensity I, which is found by solving the radiative transfer equation without scattering into the direction of the radiation propagation $\mathbf{\Omega}$ [26]:

$$\nabla \cdot \mathbf{\Omega} I + \kappa I = \kappa \frac{\sigma T^4}{\pi} \tag{10}$$

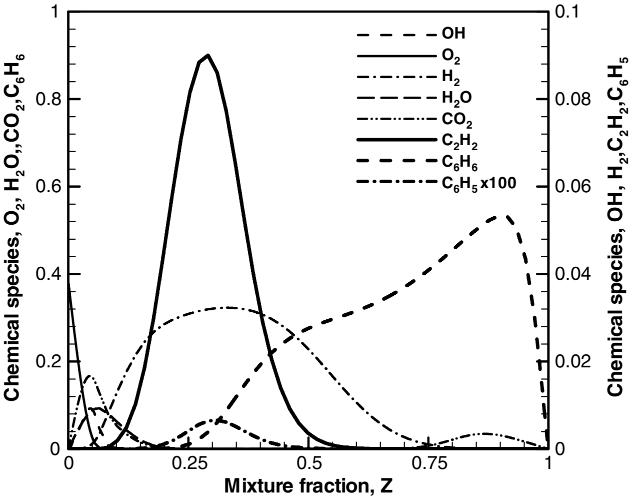

Fig. 2 State relation between chemical species and mixture fraction.

The gas-phase contribution to the gains and losses of heat via radiation, $-\nabla \cdot q_r$, in the energy equation (4) is calculated from a discrete expression [22]:

$$-\nabla \cdot q_r = -\int_{4\pi} \nabla \cdot \mathbf{\Omega} I \cdot \mathrm{d}\Omega \approx \kappa \left(\sum_{l=1}^{L} w^l I^l - 4\sigma T^4 \right) \tag{11}$$

The radiation propagation $\mathbf{\Omega}$ is limited to the computational domain. The solid wall is considered as a gray diffuse one, and the boundary condition for the radiation intensity leaving a wall is determined according to the wall emissivity and its surface temperature [26]. The calculation of the gray absorption coefficients κ of a sooting diffusion flame is based on the work of Grosshandler (RadCal) [27].

D. Soot Formation and its Oxidation

The semi-empirical soot model is based on the two time-dependent conservation equations for soot-particle number N (particles/m^3) and soot mass density M (kg/m^3):

$$\frac{\partial \rho N}{\partial t} + \frac{\partial [\rho N (u_i + u_i^{\mathrm{th}})]}{\partial x_j} - \frac{\partial}{\partial x_j}\left(\frac{\mu}{Sc} \frac{\partial N}{\partial x_j} \right) = \dot{\omega}_{N,\mathrm{inc}} + \dot{\omega}_{N,\mathrm{coa}} \tag{12}$$

$$\frac{\partial \rho M}{\partial t} + \frac{\partial [\rho M (u_i + u_i^{\mathrm{th}})]}{\partial x_j} - \frac{\partial}{\partial x_j}\left(\frac{\mu}{Sc} \frac{\partial M}{\partial x_j} \right) = \dot{\omega}_{M,\mathrm{inc}} + \dot{\omega}_{M,\mathrm{gro}} + \dot{\omega}_{M,\mathrm{oxi}} \tag{13}$$

where u_i^{th} is the thermophoretic velocity component:

$$u_i^{\mathrm{th}} = -0.54 \frac{\mu}{\rho} \frac{\partial \ln T}{\partial x_i} \tag{14}$$

The first term in Eq. (12) represents the rate of soot-particle inception, and the second term represents the soot coagulation. The second term in Eq. (13) represents the surface growth of soot, and the last term represents the soot oxidation rate.

Several theoretical and experimental works [17,18,20] highlight the importance of PAH as result of intermediary reactions in soot inception processes. Hall et al. [20] developed a soot inception model, which is based on the formation rates of two- and three-ringed aromatics ($C_{10}H_7$ and $C_{14}H_{10}$) from acetylene (C_2H_2), benzene (C_6H_6), and the phenyl radical (C_6H_5). The growth mechanism of PAH is composed of consecutive repeated reactions that can be classified in a two-step mechanism, called HACA (H-abstraction-C_2H_2-addition). The first step is an abstraction mechanism of hydrogen:

$$2C_2H_2 + C_6H_5 \rightarrow C_{10}H_7 + H_2 \tag{15}$$

The second step is the addition reaction of acetylene:

$$C_2H_2 + C_6H_6 + C_6H_5 \rightarrow C_{14}H_{10} + H_2 + H \tag{16}$$

Based on the laminar flame data, the resulting inception rate is expressed as

$$\dot{\omega}_{N,\mathrm{inc}} = \frac{8N_A}{M_p} \left\{ c_2 \left[\rho^2 \left(\frac{Y_{C_2H_2}}{W_{C_2H_2}} \right)^2 \frac{Y_{C_6H_6} W_{H_2}}{W_{C_6H_6} Y_{H_2}} \right] e^{-\frac{4378}{T}} + c_3 \left[\rho^2 \frac{Y_{C_2H_2} Y_{C_6H_6} Y_{C_6H_5} W_{H_2}}{W_{C_2H_2} W_{C_6H_6} W_{C_6H_5} Y_{H_2}} \right] e^{-\frac{6390}{T}} \right\} \tag{17}$$

$$\dot{\omega}_{M,\mathrm{inc}} = \frac{M_p}{N_A}\dot{\omega}_{N,\mathrm{inc}} \tag{18}$$

where c_2 ($127 \times 10^{8.88}$) and c_3 ($178 \times 10^{9.50}$) are the scaling factors.

The soot coagulation rate is determined by Lindstedt [28] based on the collision frequency defined by Puri et al. [29].

$$\dot{\omega}_{N,\mathrm{coa}} = -\left(\frac{24R}{\rho_{\mathrm{soot}}N_A}\right)^{1/2}\left(\frac{6}{\pi\rho_{\mathrm{soot}}}\right)^{1/6} T^{1/2}M^{1/6}N^{11/6} \tag{19}$$

The surface growth of soot is proposed by Frenklach et al. [30]:

$$\dot{\omega}_{M,\mathrm{gro}} = c_4\left(\rho\frac{Y_{\mathrm{C_2H_2}}}{W_{\mathrm{C_2H_2}}}\right)e^{\frac{12100}{T}}\left[(\pi N)^{1/3}\left(\frac{6M}{\rho_{\mathrm{soot}}}\right)^{2/3}\right] \tag{20}$$

where c_4 ($9000.6\ \mathrm{kg \cdot m \cdot kmol^{-1} \cdot s^{-1}}$) is a scaling factor.

The soot oxidation in Eq. (13) is assumed to proceed through two reaction steps:

$$\tfrac{1}{2}\mathrm{O_2} + \mathrm{C}_s \rightarrow \mathrm{CO} \tag{21}$$

$$\mathrm{C}_s + \mathrm{OH} \rightarrow \mathrm{CO} + \mathrm{H} \tag{22}$$

Lee et al. [31] measured and modeled the $\mathrm{O_2}$ and OH dependence of the soot oxidation in a laminar diffusion flame. By assuming that the kinetics of surface reactions are the limiting mechanism and that the particles are small enough to neglect the diffusion effect on the soot oxidation, the specific rate of soot oxidation is expressed by

$$\begin{aligned}\dot{\omega}_{M,\mathrm{oxi}} = {} & -c_5\tau\rho\frac{Y_{\mathrm{OH}}}{W_{\mathrm{OH}}}T^{1/2}(\pi N)^{1/3}\left(\frac{6M}{\rho_{\mathrm{soot}}}\right)^{2/3} \\ & - c_6\rho\frac{Y_{\mathrm{O}}}{W_{\mathrm{O}}}T^{1/2}(\pi N)^{1/3}\left(\frac{6M}{\rho_{\mathrm{soot}}}\right)^{2/3}e^{-\frac{19778}{T}}\end{aligned} \tag{23}$$

where c_5 ($105.81\ \mathrm{kg \cdot m \cdot kmol^{-1} \cdot K^{-1/2} \cdot s^{-1}}$) and c_6 ($18{,}903.51\ \mathrm{kg \cdot m \cdot kmol^{-1} \cdot K^{-1/2} \cdot s^{-1}}$) are the scaling factors, and a value of 0.13 is assigned to the collision efficiency, τ.

E. Method of Resolution

This study is performed by using the Fire Dynamics Simulator (FDS) code [22], developed by the National Institute of Standards and Technology. For studying quenching of a laminar flame, due to radiation losses, a soot model is implemented within the FDS code by the author. To ensure the accuracy of the numerical solution of the governing equations, submodel verification within the FDS code about the fluid modules and thermal radiation against the experimental data or analytical solution is presented elsewhere [22]. Moreover, for such low-Reynolds-number reacting flow, comparison between the numerical results and experimental standoff distances to validate the accuracy of FDS code has been presented in detail by Rouvreau et al. [9] and will not be repeated here.

Low-speed solvers used in FDS explicitly eliminate compressibility effects that give rise to acoustic (sound) waves for low-Mach-number flows (less than 0.3). An approximation to the equation of state is made by decomposing the pressure into a background component and a perturbation. The pressure p in the state and energy equations is replaced by the background pressure to filter out sound waves that travel at speeds that are much faster than the typical flow speeds expected in fire applications. In neither of these cases is the Boussinesq approximation invoked; the fluid is still considered thermally expandable, and the divergence is nonzero. Because of the use of the low-Mach-number approximation, the divergence of the flow, $\nabla \cdot u$, plays a very important role in the overall solution scheme. The divergence is obtained by taking the material (total) derivative of the equation of state and then substituting terms from the mass and energy conservation equations. The temperature is extracted from the density via the equation of state. A pressurelike elliptic partial differential equation is derived by taking the divergence of the momentum equation. The reason for the decomposition of the pressure term is so that the linear algebraic system arising from the discretization of pressurelike equation has constant coefficients and can be solved to machine-accuracy by a fast direct method that uses fast Fourier transforms. The relative difference between the computed and the exact solutions of the discretized Poisson (pressure) equation is on the order of 10^{-12}. The fidelity of the numerical solution of the entire system of equations is tied to the pressure/velocity coupling. Without the use of the direct Poisson solver, buildup of numerical error over the course of a simulation could produce spurious results [22].

The finite difference technique is used to discretize the partial differential physical equations. This procedure entails the subdividing of the calculation domain into a finite number of cells. The velocities (u, v, and w) are taken on the boundary of each cell, and all scalar variables are taken at cell centers. This staggered grid leads to a very efficient differencing scheme for the equations. All spatial derivatives are approximated by second-order finite differences, and the flow variables are updated in time using an explicit second-order predictor–corrector scheme. The convective terms are written as upwind-biased differences in the predictor step and downwind-biased differences in the corrector step. The thermal and material diffusion terms are pure central differences in both the predictor and corrector steps [22].

The boundary conditions are specified as follows: the inert solid surface is considered as adiabatic, and the no-slip condition is imposed by setting all velocities to zero. However, the mixture fraction Z_s at the porous burner boundaries is adjusted during the numerical iteration, according to the following conservation relationship:

$$(1 - Z_s)\dot{m}_s'' = -\frac{\mu}{Sc}\frac{\mathrm{d}Z_s}{\mathrm{d}n} - \Delta t u_s\frac{\mathrm{d}(\dot{m}_s'' Z_s)}{\mathrm{d}n} \tag{24}$$

where Δt is the time step and u_s the fuel-injection velocity (m/s). At the free boundaries, zero-gradient conditions are used for the far-field boundary values of the mass fractions.

III. Results and Discussions

In the experiment, microgravity conditions are attained by means of parabolic flights that provide a gravity level of 10^{-3} g during 22 s. Porous burners have been used regularly in an attempt to simplify experiments by avoiding the coupling between heat feedback from the flame and fuel supply so that longer experimentation time can be achieved. Although a zero-gravity numerical simulation is performed, the fluid and combustion equations are coupled through the contributions to the divergence of the flow, which include the heat release rate due to combustion and the net heat flux from thermal conduction and radiation. The sketch of the basic configuration is displayed in Fig. 3. A steady diffusion flame is stabilized in a boundary layer of an oxidizer stream flowing over a porous flat plate with fuel injection. The parameters varied are the oxidizer molar fraction X_{O2}, varying from 0.21 (0.79 nitrogen) to 0.35, and fuel/freestream velocities. The pyrolysis products of a condensed fuel are simulated by injecting ethylene with a weak velocity V_F, varying from 0.003 to 0.005 m/s, through a porous burner, which is characteristic of those expected from condensed-fuel pyrolysis and oxidizer flow. The fuel temperature of 300 K and the atmospheric pressure of $P = 1$ atm are imposed at the porous burner boundaries, corresponding to the experimental conditions [8]. An oxidizer flows parallel to the surface with a constant velocity V_{ox}. The dimensions of the computational domain, as shown in Fig. 3, are $8Lp$ in the windward direction and $4Lp$ in both the lateral and normal directions, so that boundary conditions can be set to conform as much as possible to the experimental configuration. The grid system contains $240 \times 80 \times 60$ cells, and cells of 1 mm are concentrated around the reacting zone. Convergence is addressed by varying the grid spacing to ensure that the results are not dependent on them. The resolution tests indicated that the computations are grid-independent when the cell dimensions are lower than 3 mm.

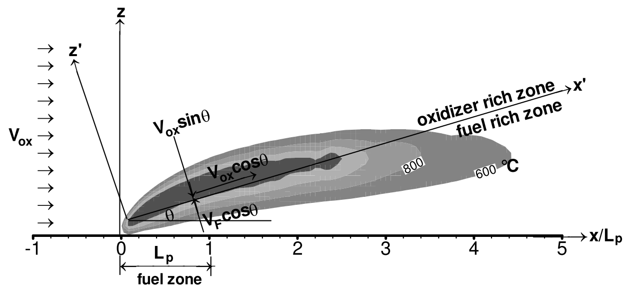

a) Calculated isocontours of the temperature (side view)

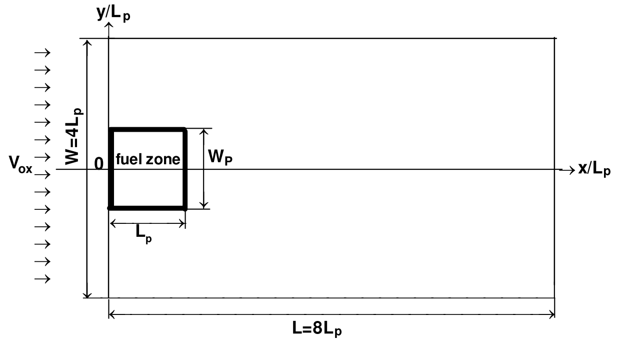

b) Disposition of the fuel zone (top view)

Fig. 3 Computational domain and the coordinate system.

A. Evaluation of the Numerical Approach at a Small Fuel Size ($L_p = 0.05$ m)

By conducting experiments under microgravity conditions, the dominant effect of buoyancy was avoided, and freestream velocities below 0.2 m/s could be studied. The experimental setup in microgravity conditions corresponds to a small square porous burner ($L_p = W_p = 5$ cm; see Fig. 3b), due to strict safety measures during the parabolic flight [7,8]. This square porous burner is embedded in the plane at $z = 0$, centered in the y direction and at 5 cm from the inlet of a large enclosed combustion chamber. As shown in Figs. 4a and 4b, the flame and soot in the cross section at the trailing edge display a 3-D behavior. Under microgravity conditions, the diffusion flame in the cross-stream plane is almost located in the pyrolysis zone. The extent of soot in the cross-stream plane is narrower than the pyrolysis zone, due to soot oxidation. A stable symmetrical soot formation is generated; however, the transverse diffusion in the presence of crossflow causes distortions of the temperature distribution. Only the soot volume fraction and flame shape on the median plane are measured and are thus available for validating the numerical models. Figure 5 shows the comparison between the predicted and measured soot volume fractions across the height z at various axial locations $x/L_p = 0.5, 1, 1.5, 2$ for $V_{\text{ox}} = 0.25$ m/s and $V_F = 0.005$ m/s. The PAH inception model correctly reproduces the general shape of the experimentally determined profiles of soot volume fraction. By looking at their locations, the measured peak is placed just above the plate surface with 3 mm, and the calculated peak occurs with 5 mm. It is noted that the computations overpredict the vertical stratification present in the experiment and, consequently, the soot-layer thickness. Globally, there is satisfactory agreement between experiment and computation for soot peak value (about 5×10^6) for the present range of experimental flow rates.

For a global description of soot production along the x axis, the soot volume fraction is integrated over the soot layer, as follows:

$$F_{\text{soot}}(x) = \int_{z=0}^{z\,\max(x)} f_{\text{soot}}(x, z)\,\mathrm{d}z \tag{25}$$

where $Z_{\max}(x)$ is the height, and so $f_{\text{soot}}(x, z) = 0$ for $z > Z_{\max}(x)$ at a given x. Three oxidizer ($V_{\text{ox}} = 0.06$, 0.125, and 0.25 m/s) and fuel ($V_F = 0.003$, 0.004, and 0.005 m/s) velocities overlapping the range of those used in the experiments [8] are discussed for their effects on F_{soot}. The simulations reproduce the aforementioned sensitivity of the experimental soot formation to both V_{ox} and V_F. A decrease of F_{soot} from 60 to $30 \times 10^6 \cdot$ mm (see Fig. 6) is induced with an increase of the oxidizer flow velocity V_{ox} from 0.06 to 0.25 m/s at a fuel-injection velocity of 0.005 m/s. An inverse dependence of the soot formation on the mainstream flow is predicted, and these tendencies are consistent with the experimental observation of Konsur et al. [4]. An enhancement of F_{soot} (see Fig. 7) from 20 to $38 \times 10^6 \cdot$ mm occurs with an increase of the fuel-injection velocity V_F from 0.003 to 0.005 m/s at an oxidizer velocity of 0.25 m/s. The peak values of the integrated soot volume fraction are located far away from the trailing edge ($x/L_p > 1$). Note that the extent of the measured soot is always within the zone of $x/L_p < 3$. In the experiment, the sooting behavior of the flat-plate laminar diffusion flame is characterized by using the laser-induced incandescence (LII) technique. The basic principle of LII relies on the detection of the thermal radiation from the soot particles that have been heated up to vaporization temperature by means of high-energy laser pulse. LII measurements require correction, due to attenuations of both the laser beam and the collected signal. After evaluation of the extinction, LII intensity image is converted to a soot volume fraction distribution. The accuracy of soot concentration depends on the accuracy of the proportionality constant. In addition, for the low fuel-injection velocity of $V_F = 0.003$ m/s, the flames considered have

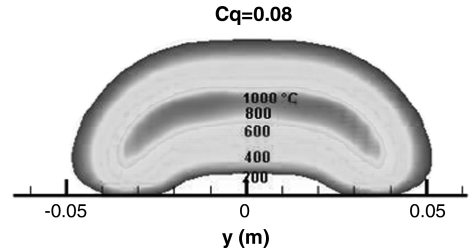

a) Temperature

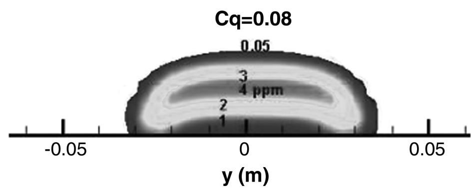

b) Soot formation

Fig. 4 Isocontours of temperature and soot in the cross section at the trailing edge.

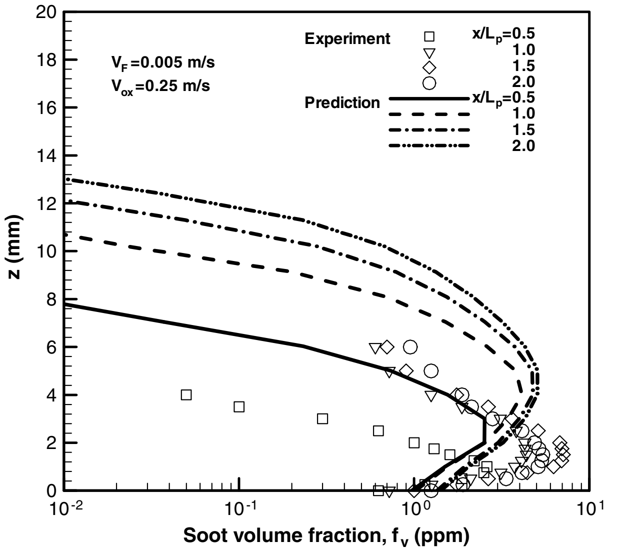

Fig. 5 Comparison between the predicted and measured soot volume fractions across the height, z, at various axial locations.

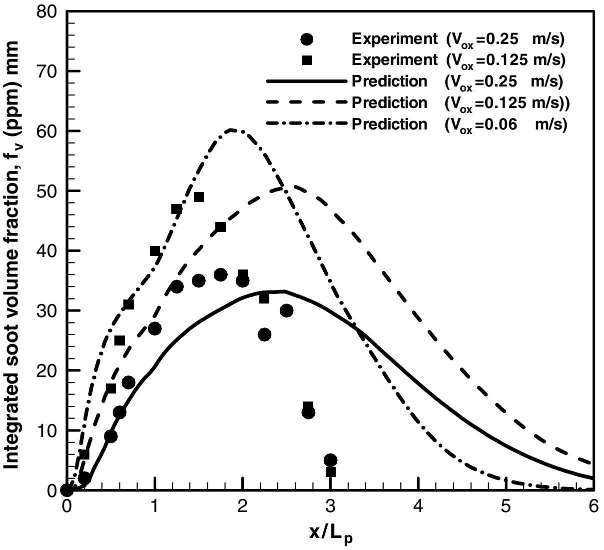

Fig. 6 Comparison between prediction and experiment for the effects of oxidizer flow velocity on the integrated soot volume fraction.

the particularity of being mostly two-dimensional. For high V_F, the flames considered develop strongly three-dimensional features far away from the trailing edge, affecting the collected signal for LII. This analysis is supported by the fact that the predicted soot profile closely follows the experimental trend for the low fuel-injection velocity of 0.003 m/s, because the soot formation occurs within the extent of the collected signal for LII. For the fuel-injection velocity beyond 0.004 m/s, the general shape of the predicted soot profiles has qualitative agreement with the experimental data. The error in numerical simulation is linked to the constants used in the semi-empirical soot model, which are experimentally determined for a given configuration. Generally, only a qualitative agreement with the measured soot volume fraction is achieved by using these standard constants [17]. It is felt that the difference is due to a combination of experimental uncertainties and the error in the numerical simulation.

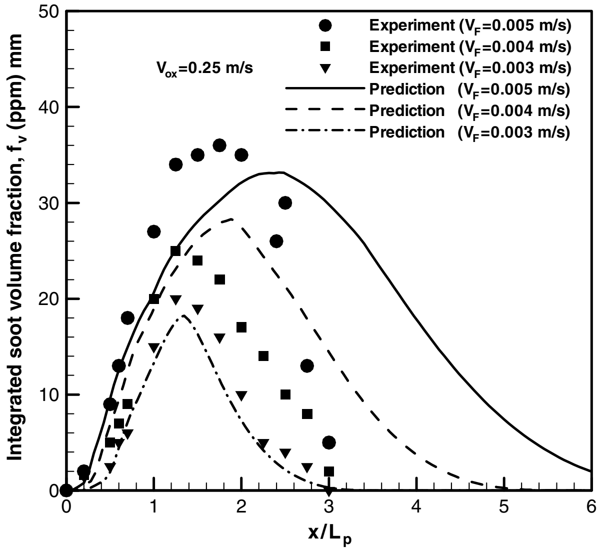

Fig. 7 Comparison between prediction and experiment for the effects of fuel-injection velocity on the integrated soot volume fraction.

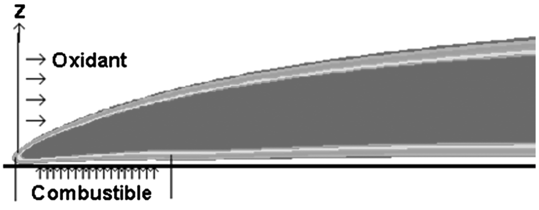

a) Without radiation

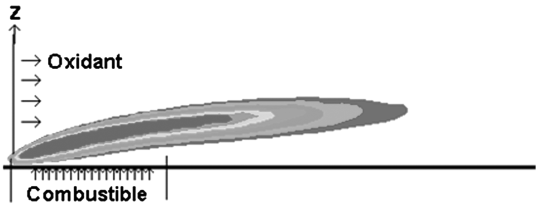

b) PAH inception model

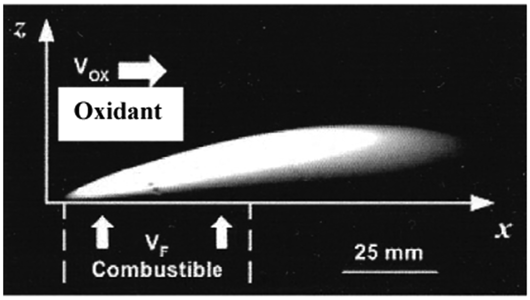

c) Experiment

Fig. 8 Effect of soot formation on the geometric characteristics of a cocurrent flame.

The effect of radiation on the geometric characteristics of a cocurrent flame is evidenced in Figs. 8a–8c. Here, the predicted visible flame shape is defined as the 600°C contour below which radiation loss is too low to affect the flame, and this definition appears to be very close to the experimental visible flame [7,8]. The experimental flame (see Fig. 8c) detaches from the trailing edge, and the leading edge remains attached to the burner surface with a parabolic nature. The experimental flame shape is correctly held by taking into account the radiation loss through the PAH inception model (see Fig. 8b). In the absence of radiation loss (see Fig. 8a), the disagreement between experiment and prediction is carried through the entire flame, becoming most evident in the quenching or extinction region near the trailing edge. This implies that the geometrical characteristics of the flame are significantly influenced by the soot formation through the radiation heat transfer.

For describing the effect of injection in the boundary layer with blowing, a dimensionless volume coefficient $C_q = V_F/V_{\mathrm{ox}}$, defined by Schlichting [32], is currently employed. This case is selected in this demonstration to clearly illustrate the peak temperature dependence on C_q at the trailing edge for two different oxygen concentrations. Both of these measured and predicted values are presented in Fig. 9. Brahmi et al. [14] argued that thermocouples perturb the flame, and thus the measured flame temperatures (550°C at $X_{\mathrm{O2}} = 0.21$ and 650°C at $X_{\mathrm{O2}} = 0.35$) clearly deviate from the real flame temperature. According to the prediction, this characteristic temperature at the trailing edge is strongly dependent on both X_{O2} and C_q, and a temperature drop of approximately 300°C occurs with a decrease of oxygen concentration from 0.35 to 0.21 at $C_q = 0.08$. The general characteristics of the flame temperature at the trailing edge include an initially gradual reduction in temperature level with C_q, followed by a rapid decrease in temperature until quenching. An increase in oxygen concentration magnifies the discrepancy between experiment and prediction, which reaches a maximum for the lowest C_q.

Figure 10 shows the ratio d_f/d_b between the flame standoff distance d_f and the boundary-layer thickness d_b. Here, we use the visible flame shape ($T > 600°\mathrm{C}$) to define the horizontal flame length L_f from the leading edge (see Fig. 3). The flame standoff distance d_f is the distance between the plate and the flame sheet, where oxygen and fuel is delivered in stoichiometric proportions corresponding to the maximum heat release rate (HRR). This thickness d_b is defined as

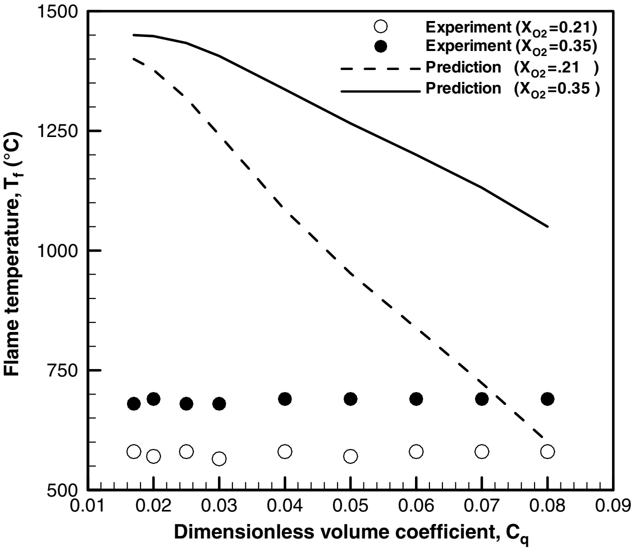

Fig. 9 Evolution of the flame temperature at the trailing edge as a function of C_q.

the distance above the surface, where the parallel component of velocity reaches 99% of the main flow velocity. The flame leading edge is positioned very close to the porous-plate edge, and the flame establishes inside the viscous boundary layer ($d_f/d_b < 1$), denoting the importance of diffusion there. For C_q beyond the value of 0.02, the 3-D effects behind a finite fuel zone [9] are of importance, and as a consequence of the lateral entrainment, the flame is significantly lifted above the boundary layer ($d_f/d_b > 1$). Both thermal expansion and interacting flow between fuel and oxidizer become less obvious, as C_q is below 0.02, and thus the two-dimensional flow structure is approximate. In this case, after heat release ceases (i.e., after quenching), heat dissipation causes the flame temperature and magnitude of the ratio d_f/d_b to decrease until the flame migrates toward the boundary layer ($d_f/d_b < 1$) at $x/L_p > 3$.

B. Flame Behavior Along a Semi-Infinite Fuel Zone ($L_P \to \infty$)

Most of the work [13,32,33] in a reactive boundary layer with blowing concentrated on the description of flame standoff over a semi-infinite fuel surface ($L_P \to \infty$). This case is also selected in this demonstration to clearly illustrate the effect of radiation on the flame characteristics over a large fuel size. For low-Reynolds-number flow, two regimes have been clearly identified by Rouvreau et al. [9]. For larger values of C_q (greater than 0.08), the parietal injection can lead to flow separation. Flow separation is characterized by a recirculation pattern at the trailing edge of the injector, which invalidates the use of boundary-layer approximations. In the case of flow separation, diffusion flames can only be described with a formulation that makes full account of the three-dimensionality of the flow. For the present study, low values of C_q (≤ 0.08) are considered, and the flow remains attached. Therefore, the different assumptions used within the boundary-layer formulation should be validated for conditions in which there is no separation. For the flame considered here, thermal radiation has a major influence on the flame structure. Particularly, the presence of soot particles in the combustion gas mixture greatly enhances radiation from the flame. Figure 11 shows the ratio d_f/d_b between the flame standoff distance d_f and the boundary-layer thickness d_b at $X_{O2} = 0.35$. As x increases along an infinite fuel zone, both d_f and d_b move away from the plate into an area of higher velocity, and the ratio d_f/d_b converges to one single curve and toward a constant value of 1.2, implying that the flame sheet crosses the momentum boundary layer. An asymptotical solution from the reactive boundary-layer model [13] suggests that the flame always resides within the boundary layer, and it still seems incapable of predicting this type flame. The works of Andreussi [34] concluded that the Shvab–Zel'dovich analysis is only adequate for freestream velocities higher than 1.2 m/s. Consequently, the natural constraints imposed by buoyancy in the absence of radiation heat transfer prevent complete validation of this model.

Figure 12 shows the dependence of boundary-layer thickness on both C_q and the oxygen concentration. This shows that the flow is deflected at the leading edge by thermal expansion. Although the flow never comes back to its original streamlines, it gains linear dependency with x. Initially, the boundary layer versus x-axis curves monotonically decreases with reduction in C_q, but for C_q below 0.02, it levels off, despite the oxygen concentration. This evidences an uncoupling of the momentum boundary layer from thermal expansion, due to heat combustion as the oxygen concentration increases.

Figures 13a–13c show the effects of radiation heat transfer on flame length L_f and its standoff distance for two different oxygen concentrations ($X_{O2} = 0.21$ and 0.35) as a function of C_q. As large soot is formed far away from the leading edge, resulting from flame expansion, the effect of radiative loss on the flame close to this region becomes less significant. Energy release from an exothermic chemical reaction leads to a further enhancement of the flow perturbations at the leading edge of the burner, which defines a region in which the streamwise flow is deflected from the flame region. Thus, with or without radiation, the flame leading edge is positioned

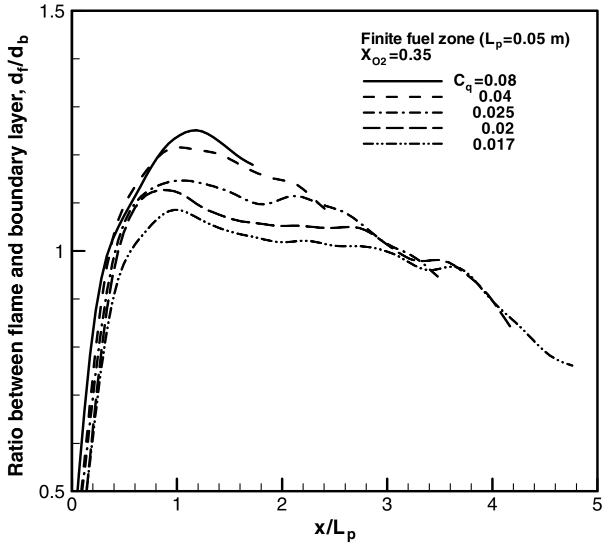

Fig. 10 Ratio between flame standoff distance and boundary-layer thickness for different C_q along a finite fuel zone.

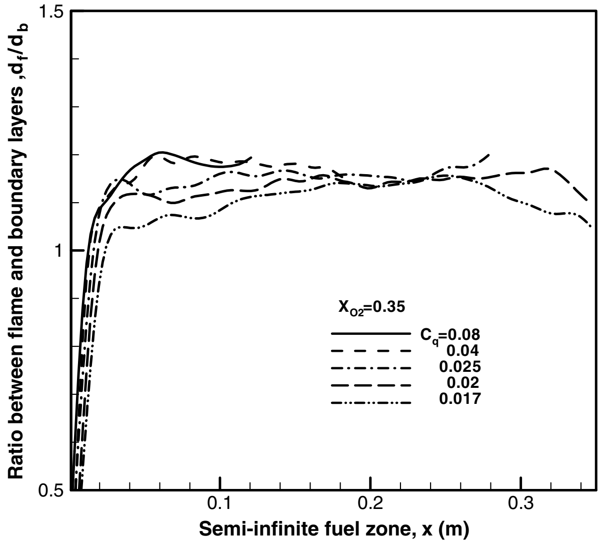

Fig. 11 Ratio between flame standoff distance and boundary-layer thickness for different C_q along a semi-infinite fuel zone.

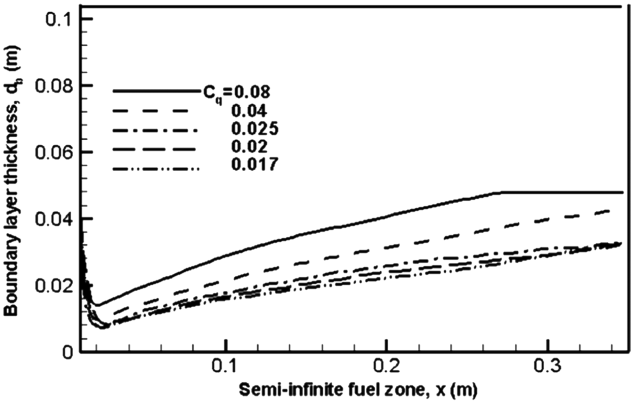

a) With radiation at X_{O2}=0.35

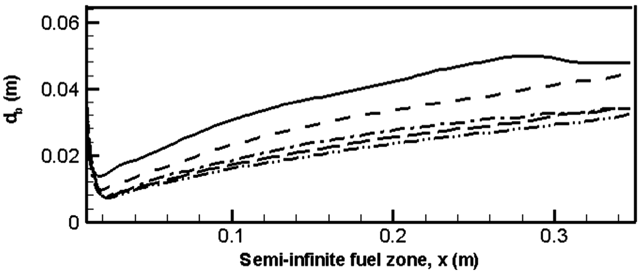

b) With radiation at X_{O2}=0.21

Fig. 12 Boundary-layer thicknesses over a semi-infinite fuel zone for different C_q.

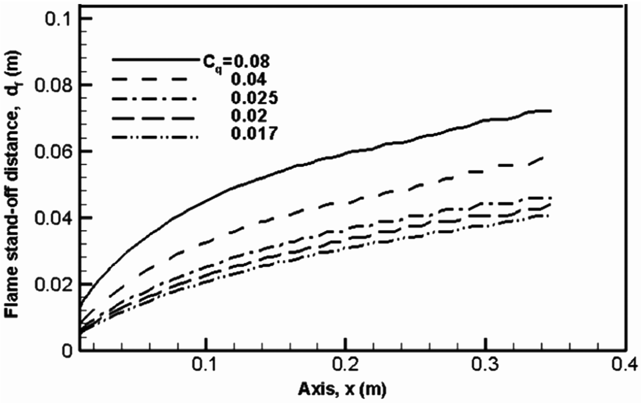

a) Without radiation

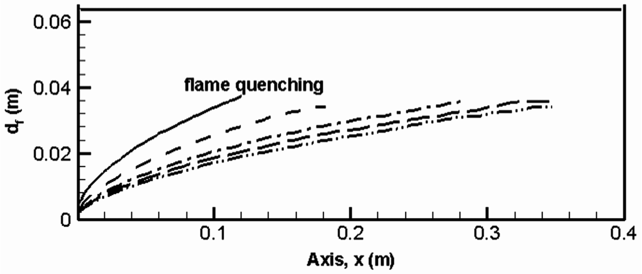

b) With radiation at X_{O2}=0.35

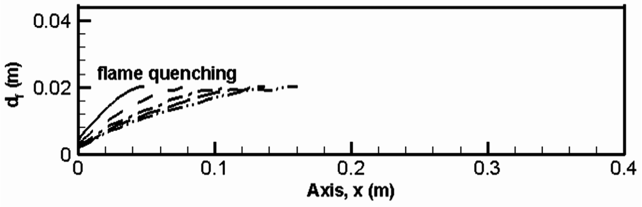

c) With radiation at X_{O2}=0.21

Fig. 13 Flame standoff distance and its length along the x axis for different C_q.

very close to the porous-plate edge, showing the parabolic nature of this region, due to absence of the streamwise flow. The curvature of the leading edge is more pronounced for C_q beyond 0.02, and below this value, the visible flame is characterized by a small curved zone close to the leading edge. The flame is fully detached from the burner downstream, implying the lack of oxygen inside the boundary layer, followed by a linear zone. The discrepancy grows with the downstream distance from the leading edge, and the flame standoff distance is much larger, as the flame is adiabatic. Without radiation (see Fig. 13a), an infinite flame length along the fuel zone ($L_P \rightarrow \infty$) is numerically reproduced, independent of C_q. When the flame quenching occurs, the flame stops consuming reactant, and so excessive fuel is accumulated. Thus, this diffusion flame is open-tip, because quenching occurs due to radiation loss before the fuel is fully consumed. It is found that a decrease of C_q results in an increase in the flame length (see Fig. 13b), due to reduction in soot formation (see Fig. 6). The flames converge to the same standoff distance as x increases for $C_q < 0.02$. The oxygen concentration seems to have little effect on the inclination of the flame close to the leading edge, but as the distance downstream increases, both flames at $X_{O2} = 0.21$ and 0.35 are significantly different. The results indicate that less distance is required to reach the quenching at $X_{O2} = 0.21$, which occurs at $x = 0.05$ m for $X_{O2} = 0.21$ and at $x = 0.12$ for $X_{O2} = 0.35$ at $C_q = 0.08$, for example. That means that for low oxygen concentration, and thus lower temperature, the flame enters the quenching earlier. An increase in oxygen concentration still leads to a larger standoff distance, showing that diffusion is less important than expansion and convection. For C_q below 0.02, thermal expansion dominates, and hotter flames at $X_{O2} = 0.35$ have a larger standoff distance than colder flames at $X_{O2} = 0.21$. As the experimental observation [7,8], the predicted flame standoff distance is an order of magnitude larger than that predicted by a Shvab–Zel'dovich analysis, as described by Emmons [33] for a reacting boundary-layer flow with blowing.

When convection, natural or forced, carries soot toward the flame, soot-particle trajectories approximately follow the gas movement, and so it becomes incandescent and glows or burns. When diffusion or thermal expansion dominates, soot particles cannot approach the flame, due to the thermophoretical effects. This simple explanation seems to well describe the experimental observation of Fujita et al. [35] for a laminar boundary-layer diffusion flame in microgravity. Figure 14 shows an illustration of the predicted ratio d_{soot}/d_b between the soot standoff distance d_{soot} and the boundary-layer thickness d_b along a semi-infinite fuel zone. Note that the location of the soot formation for such flame is practically independent of both the fuel size and oxygen concentration. Contrary to the flame standoff distance (see Fig. 13), the maximum soot formation always occurs inside the boundary layer ($d_{\mathrm{soot}}/d_b < 1$) far away from the stoichiometric line. This is evidenced by a significant deviation of soot particles from the stoichiometric line, due to the dominant thermal expansion that prevents soot particles approaching the flame. The peak soot production is placed just over the plate surface in the fuel-rich zone (see Fig. 5), and its location does not follow the response of flame standoff to changes in mainstream parameters. Numerical simulations incorporating the soot formation confirmed the preceding experimental observations [7,8].

C. Influences of Soot Formation on the Flame Behavior

Gas-phase quenching or extinction phenomena are often described using the Damköhler number, which is the ratio of a characteristic residence time τ_{re} over a characteristic chemical time τ_{ch}:

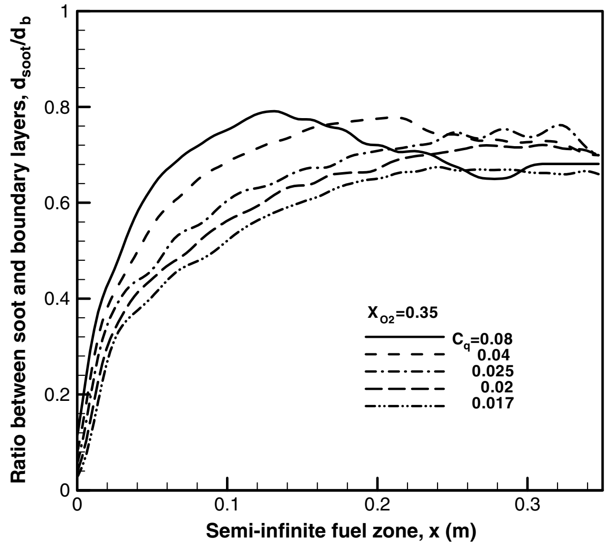

Fig. 14 Ratio between soot and boundary-layer thicknesses over a semi-infinite fuel zone for different C_q.

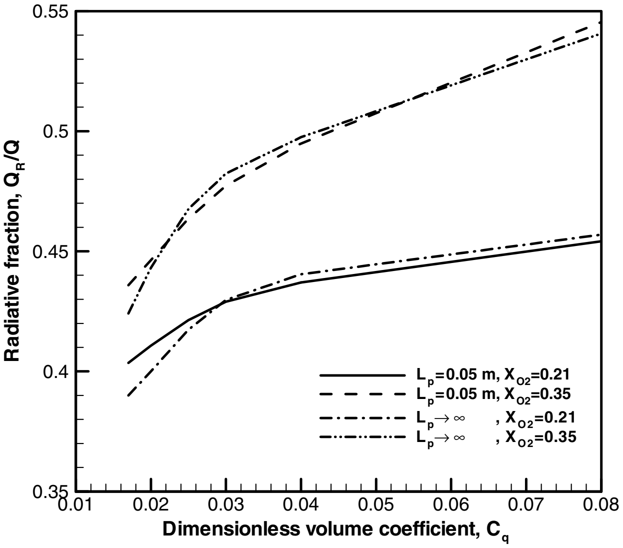

Fig. 16 Evolution of the radiative fraction as a function of C_q.

$$\bar{D}_a = \frac{\tau_{\rm re}}{\tau_{\rm ch}} = \frac{\rho_\infty A T_f \exp(-E/RT_f)}{(V_{\rm ox}^2/\alpha_\infty)} \tag{26}$$

The effect of soot formation on the flame temperature T_f, which is the dominant factor in Eq. (26), is presented in Fig. 15. It can be seen that without radiative heat transfer, an adiabatic flame temperature of 2000°C is numerically reproduced. As radiative losses are dominant for this heavily sooting flame, the temperature rise occurs behind the leading edge, because less soot is formed until the temperature continuously falls off, due to large soot formation. A temperature drop implies longer chemical times, and thus lower Damköhler numbers, until quenching occurs around a soot concentration of $F_{\rm soot} \approx 50 \times 10^6 \cdot$ mm, consistent to the smoke-point concept [4,5]. This critical $F_{\rm soot}$ is of great importance for evaluating the flame length of a cocurrent flame spread. In contrast to extinction at small Damköhler numbers, the end of heat generation for these flames is due to soot formation resulting from flame expansion through radiation losses.

Radiative extinction for such a flame is unlikely in normal gravity, because buoyancy enhances mixing and reduces residence times, and so the radiative loss fraction is below 0.1. In the absence of natural convection, radiative loss becomes the primary variable triggering reactive zone [3]. The radiative fraction, Q_R/Q, where Q_R is the radiative heat loss rate and Q calculated heat generation rate is plotted versus C_q in Fig. 16 for two fuel sizes ($L_p = 0.05$ m and $L_P \to \infty$) and oxygen concentrations ($X_{\rm O2} = 0.21$ and 0.35). Because the radiative heat loss is a temperature-sensitive volumetric loss mechanism, the loss rate depends on the volume of the high-temperature region, which is given approximately by

$$V_{f,\rm visible} = L_f \times \delta_f \times W_f \tag{27}$$

where δ_f and W_f are, respectively, the visible flame thickness and width. The plot of Q_R/Q indicates that in all cases, this ratio is higher than 0.4 and increases rapidly with C_q but then slowly for large C_q (greater than 0.04). Thus, radiative quenching can be important in microgravity. For such quasi-steady flames, the stronger the oxygen concentration, the greater the radiation loss, due to increase in flame volume (see Fig. 13), which is proportional to the oxygen concentration. An important observation of this work is that the ratio Q_R/Q is solely a function of $X_{\rm O2}$ at a fixed C_q and is practically independent of the fuel size L_p. The combustion efficiency (see Fig. 17), which is determined from the ratio Q/Q_T (where $Q_T = \dot{m}_s'' L_p W_p H_c$ denotes the theoretical heat release rate), decreases monotonically with C_q. An interesting feature of this figure is that an improvement of combustion efficiency is driven by a finite fuel size ($L_p = 0.05$ m) as a consequence of the lateral entrainment behind a finite fuel zone. The work of Rouvreau [9] confirmed the presence of

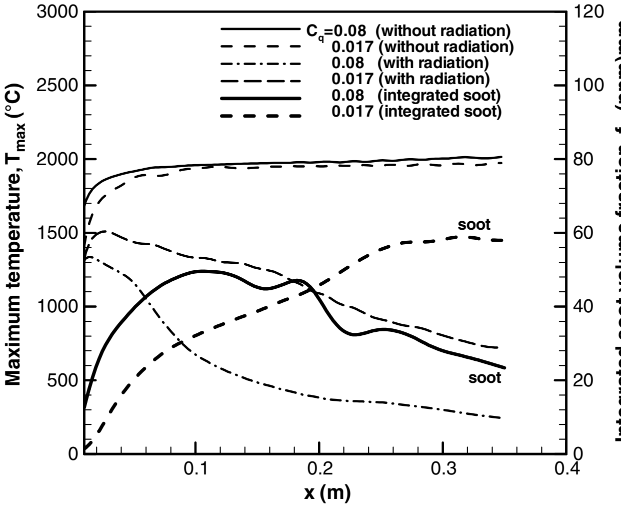

Fig. 15 Effect of the radiation on the maximum gas temperature over a semi-infinite fuel zone.

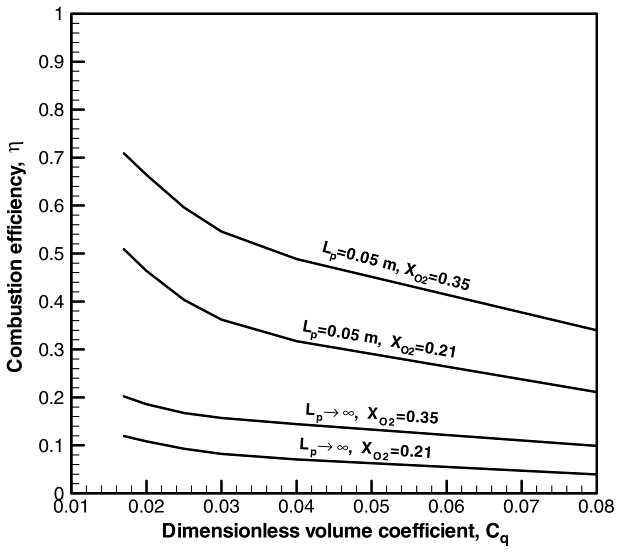

Fig. 17 Evolution of the combustion efficiency as a function of C_q.

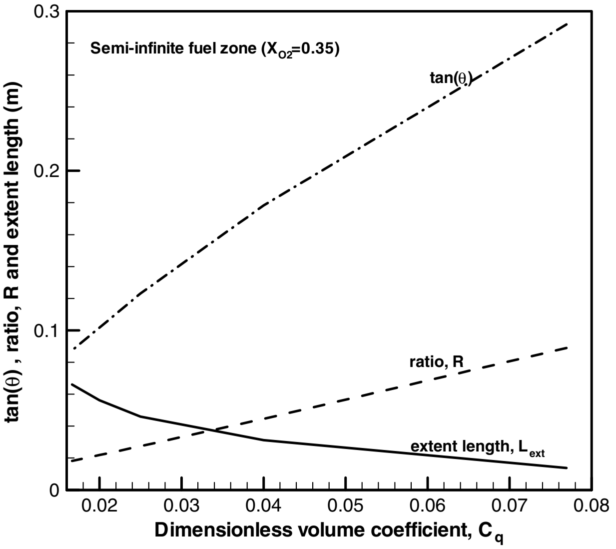

Fig. 18 Evolution of fuel accumulation extent, characteristic time, and flame slope as a function of C_q.

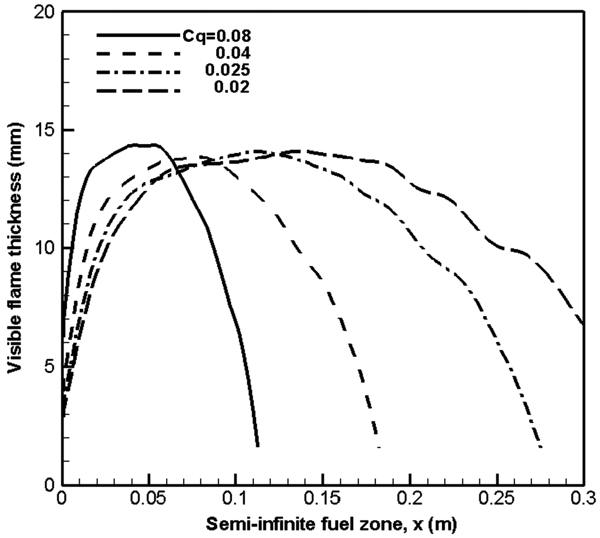

Fig. 20 Thickness of the visible flame over a semi-infinite fuel zone for different C_q.

a 3-D flow pattern generated by the fuel injection through a finite fuel zone. A semi-infinite fuel zone ($L_P \to \infty$) eliminates the recirculation zone at the trailing edge of the injection zone and, as a consequence, reduces the oxygen supply to the boundary layer, resulting in a dramatic reduction in combustion efficiency. On the other hand, the combustion efficiency falls off with a reduction in oxygen concentration, despite the fuel size.

The flame is deflected at the leading edge by thermal expansion with a parabolic nature, but once this deflection has occurred, it gains the linear dependency with x. As an illustration, following the assumption of the pioneering work [2] related to a diffusion flame in microgravity, the flame standoff is approximately described by a straight line (see Fig. 3a), with a slope defined by the expression $\tan\theta = d_f/L_f$. As shown in Fig. 18, a reduction of C_q results in a decrease in the flame slope, which thus approaches the fuel surface, denoting the importance of diffusion. At this point, fuel and oxidizer are transported toward the mixing zone by convection, but within this zone, diffusion determines the flame location. The predicted flame thickness ε is calculated from the zone where oxygen and fuel are delivered in stoichiometric proportions corresponding to the maximum HRR. The characteristic time is defined as $\tau = S\varepsilon^2/DY_{\mathrm{o},\infty}$, where S is the stoichiometric oxidizer-to-fuel ratio by mass, implying that fuel and oxidizer need to diffuse in stoichiometric proportions through the flame thickness ε. As shown in Fig. 19, the predicted flame thickness changes slightly with the mainstream parameter; for all values of fuel and oxidizer velocities studied, $\varepsilon \approx 1.2$ mm and thus $\tau \approx 0.22$ s. That means that the reaction between the z components (see Fig. 3a) of fuel, $V_F \cos\theta$, and oxidizer, $V_{\mathrm{ox}} \sin\theta$, occurs in a reaction zone of approximately 1.2 mm in a period of about 0.22 s. However, thickness δ_f of the predicted visible flame (600°C contour), as shown in Fig. 20, strongly depends on the mainstream parameter. Along a semi-infinite fuel zone, thickness δ_f increases first to a maximum value of 14 mm and then decreases toward zero. It is found that the maximum thickness δ_f is about 13 times that of flame sheet ε, independent of the mainstream parameter. In the x direction (see Fig. 3a), oxidizer and fuel separate from each other with a velocity given by $V_{x'} = V_{\mathrm{ox}} \cos\theta - V_F \sin\theta$. The ratio $R = \varepsilon/\tau V_{x'}$ tells us if fuel and oxidizer arriving parallel to the x axis will react ($R > 1$) or if oxidizer will escape before being able to react with the fuel ($R < 1$). Evolution of the ratio R as a function of C_q (see Fig. 18) indicates that its value is much lower than 1, implying that fuel accumulates at the stoichiometric line. The extent of the fuel accumulation is determined by the distance the oxidizer can be convected along the stoichiometric line before it can diffuse a distance ε; therefore, it can be approximately determined by $L_{\mathrm{ext}} = \tau V_{\mathrm{ox}} \cos\theta$. The value of L_{ext} is inversely proportional to C_q and ranges from 1.5 cm for the largest C_q to 6 cm for the smallest one. Figure 21 shows the predicted length of the reactive zone for two different fuel sizes ($L_p = 0.05$ m and $L_P \to \infty$) and oxygen concentrations ($X_{\mathrm{O2}} = 0.21$ and 0.35). Figure 21 shows that the reactive zone is proportional to the extent of the fuel accumulation with a proportionality constant that depends on the fuel size and oxygen concentration. In the simulation, the reactive zone is established as the locus of the peak energy release zone,

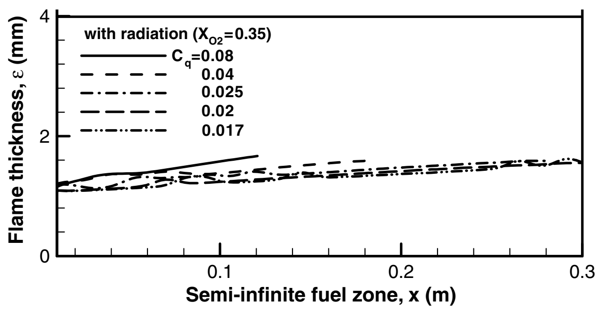

Fig. 19 Thickness of the flame sheet over a semi-infinite fuel zone for different C_q.

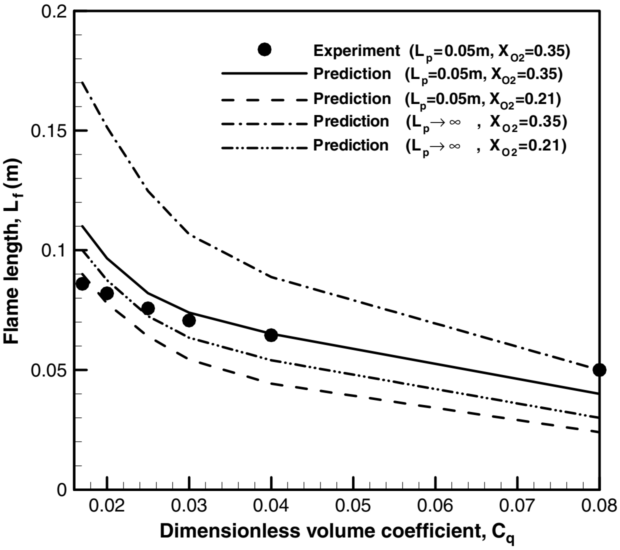

Fig. 21 Evolution of the reactive zone length as a function of C_q.

corresponding to a peak temperature of about 1100 K, which is significantly lower than for kinetic extinction. The measured reactive length is available only at $X_{O2} = 0.35$ and $L_p = 0.05$ m and is presented in Fig. 21 as a reference. Note that the visible flame length (see Fig. 13) does not necessarily match the reactive zone, due to the presence of soot with the high temperature level ($T > 600°C$). Thus, the reactive zone has a shorter length than that of a visible flame. Both experiment and numerical computations show that length of the reactive zone decreases monotonically with a reduction in C_q, despite the fuel size and oxygen concentration. The radiative fraction increases with C_q (see Fig. 16), and the combustion efficiency decreases (see Fig. 17), such that reduction in reactive zone with C_q is a consequence of a gradual increase in radiation loss coupled with a gradual decrease in combustion efficiency. At low oxygen $X_{O2} = 0.21$, a large fuel size ($L_P \to \infty$) has a shorter reactive length, implying that flame extinguishes earlier than at $X_{O2} = 0.35$, due to a dramatic reduction in combustion efficiency. Despite the oxygen concentration, the reactive zone exceeds a finite fuel zone ($L_p = 0.05$ m) at the trailing edge, reaching a length of about $2L_p$ for the lowest value of C_q; due to the high combustion efficiency, even the flame suffers more radiative loss.

IV. Conclusions

This numerical study highlights the importance of soot formation on the quenching of a microgravity diffusion flame established over a flat plate. The soot inception is controlled by the benzene formed from acetylene, and the behavior of the soot production as a function of C_q is reasonably well predicted by using the PAH inception model. The major findings are as follows.

1) For a low-Reynolds-number reacting flow in microgravity, the flame establishes outside the viscous boundary layer, whereas the soot resides within the boundary layer far from the stoichiometric line, implying that diffusion is less important than expansion and convection.

2) A large C_q favors soot formation and, consequently, flame quenching, due to a significant radiative heat loss.

3) The diffusion flame is open-tip, because quenching occurs before the fuel is fully consumed, and so fuel accumulates at the stoichiometric line.

4) As a consequence, the visible flames ($T > 600°C$) significantly exceed at the trailing edge for C_q below 0.02, reaching a length of greater than five times the fuel zone. Maximum visible flame thickness is about 13 times that of the flame sheet, independent of the mainstream parameter. A maximum in both the visible flame length and thickness for oxidizer velocities below those encountered in natural convection represents a greater hazard for fire safety in spacecraft.

5) The radiative loss fraction is solely a function of oxygen concentration at a fixed C_q, and is practically independent of the fuel size. The combustion efficiency also falls off with a reduction in oxygen concentration, despite the fuel size.

6) Radiative heat losses can drive flame quenching, and the heat release rate decreases as the oxygen concentration decreases. Therefore, at low oxygen concentration, it is this combination that leads to earlier quenching.

These results are valid only for gaseous fuel and oxidizer and should not be directly extrapolated to condensed-fuel burning. Condensed-fuel vaporization has a stronger effect on the structure of the flow only downstream of the leading edge. Coupling between heat feedback from the flame, fuel supply, and flame geometry create an insurmountable difficulty during the parabolic flight. Ongoing work will account for the PAH inception model for predicting flame spread over a condensed-fuel surface in microgravity.

References

[1] Ross, H. D., *Fire in Free Fall: Micro-Gravity Combustion*, Academic Press, San Diego, CA, 2001, pp. 299–418.

[2] Torero, J. L., Bonneau, L., Most, J. M., and Joulain, P., "The Effect of Gravity on a Laminar Diffusion Flame Established over a Horizontal Plate," *25th Symposium (International) on Combustion*, Combustion Institute, Pittsburgh, PA, 1994, pp. 1701–1709.

[3] Olson, S. L., and T'ien, J. S., "Buoyant Low-Stretch Diffusion Flames Beneath Cylindrical PMMA Samples," *Combustion and Flame*, Vol. 121, No. 3, 2000, pp. 439–452.
doi:10.1016/S0010-2180(99)00161-3

[4] Konsur, B., Megaridis, C. M., and Griffin, D. W., "Soot Aerosol Properties in Laminar Soot-Emitting Microgravity Nonpremixed Flames," *Combustion and Flame*, Vol. 118, No. 4, 1999, pp. 509–520.

[5] Markstein, G. H., and De Ris, J., "Radiant Emission and Absorption by Laminar Ethylene and Propylene Diffusion Flame," *20th Symposium (International) on Combustion*, Combustion Institute, Pittsburgh, PA, 1985, pp. 1637–1646.

[6] T'ien, J. S., "The Possibility of a Reversal of Flammability Ranking from Normal Gravity to Microgravity," *Combustion and Flame*, Vol. 80, Nos. 3–4, 1990, pp. 335–357.
doi:10.1016/0010-2180(90)90111-4

[7] Legros, G., Joulain, P., Vantelon, J. P., Fuentes, A., and Torero, J. L., "Soot Volume Fraction Measurements in a Three-Dimensional Laminar Diffusion Flame Established in Microgravity," *Combustion Science and Technology*, Vol. 178, Nos. 4–6, 2006, pp. 178–180.
doi:10.1080/00102200500271344

[8] Fuentes, A., Legros, G., Claverie, A., Joulain, P., Vantelon, J. P., and Torero, J. L., "Influence of the Oxidizer Velocities on the Sooting Behaviour of Nonbuoyant Laminar Diffusion Flame," *31st Symposium (International) on Combustion*, Combustion Institute, Pittsburgh, PA, 2007, pp. 2685–2692.

[9] Rouvreau, S., Torero, J. L., and Joulain, P., "Numerical Evaluation of Boundary Layer Assumptions for Laminar Diffusion Flames in Micro Gravity," *Combustion Theory and Modelling*, Vol. 9, No. 2, 2005, pp. 137–158.
doi:10.1080/13647830500098381

[10] Ha, J. S., Shim, S. H., and Shin, H. D., "Boundary Layer Diffusion Flame over a Flat Plate in the Presence and Absence of Flow Separation," *Combustion Science and Technology*, Vol. 75, 1991, pp. 241–260.
doi:10.1080/00102209108924091

[11] Ramachandra, A., and Raghunandan, B. N., "Investigations on the Stability and Extinction of a Laminar Diffusion Flame over a Porous Flat Plate," *Combustion Science and Technology*, Vol. 36, 1984, pp. 109–121.
doi:10.1080/00102208408923728

[12] Santa, K. J., Chao, B. H., and Sunderland, P. B., "Radiative Extinction of Gaseous Spherical Diffusion Flames in Microgravity," *Combustion and Flame*, Vol. 151, 2007, pp. 665–675.
doi:10.1016/j.combustflame.2007.08.009

[13] Liu, S., Catalin, G., and Fotache, "Boundary Layer Modelling of Reactive Flow over a Porous Surface with Angled Injection," *Combustion and Flame*, Vol. 154, 2008, pp. 378–386.
doi:10.1016/j.combustflame.2008.05.022

[14] Brahmi, L., Vietoris, T., Rouvreau, S., Joulain, P., David, L., and Torero, J. L., "Microgravity Laminar Diffusion Flame in a Perpendicular Fuel and Oxidizer Stream Configuration," *AIAA Journal*, Vol. 43, No. 8, 2005, pp. 1725–1733.
doi:10.2514/1.13442

[15] Lui, F., Guo, H. S., Gregory, J., Smallwood, J., and Ömer, L., "Effects of Gas and Soot Radiation on Soot Formation in a Coflow Laminar Ethylene Diffusion Flame," *Journal of Quantitative Spectroscopy and Radiative Transfer*, Vol. 73, 2002, pp. 409–421.
doi:10.1016/S0022-4073(01)00205-9

[16] Leung, K. M., Lindstedt, R. P., and Jones, W. P., "A Simplified Reaction Mechanism for Soot Formation in Nonpremixed Flames," *Combustion and Flame*, Vol. 87, 1991, pp. 289–305.
doi:10.1016/0010-2180(91)90114-Q

[17] Wen, Z., Yun, S., Thomson, M. J., and Lightstone, M. F., "Modeling Soot Formation in Turbulent Kerosene/Air Jet Diffusion Flames," *Combustion and Flame*, Vol. 135, 2003, pp. 323–340.
doi:10.1016/S0010-2180(03)00179-2

[18] Vovelle, C., Delfan, J. L., and Reuillon, M., *Soot Formation in Combustion*, Springer–Verlag, Berlin, 1994, p. 50.

[19] Anderson, H., McEnally, C. S., and Pfefferle, L. D., "Experimental Study of Naphthalene Formation Pathways in Non-Premixed Methane Flames Doped with Alkylbenzenes," *28th Symposium (International) on Combustion*, Combustion Institute, Pittsburgh, PA, 2000, pp. 2577–2585.

[20] Hall, R. J., Smooke, M. D., and Colket, M. D., "Physical and Chemical Aspects of Combustion," *A Tribute to Irvine Glassman*, edited by F. L. Dryer, and R. F. Sawyer, Gordon & Breach, New York, 1997, p. 189.

[21] Dagaut, P., and Nicolle, A., "Experimental and Detailed Kinetic Modeling Study of the Effect of Exhaust Gas on Fuel Combustion: Mutual Sensitization of the Oxidation of Nitric Oxide and Methane over Extended Temperature and Pressure Ranges," *Combustion and Flame*, Vol. 140, 2005, pp. 161–171. doi:10.1016/j.combustflame.2004.11.003

[22] Fire Dynamics Simulator, Software Package, Ver. 4, National Institute of Standards and Technology, Gaithersburg, MD, 2007.

[23] Huggett, C., "Estimation of Rate of Heat Release by Means of Oxygen Consumption Measurements," *Fire and Materials*, Vol. 4, 1980, pp. 61–85. doi:10.1002/fam.810040202

[24] Poinsot, T., and Veynante, D., *Theoretical and Numerical Combustion*, 2nd ed., Edwards, Philadelphia, 2005.

[25] Lutz, A. E., Kee, R. J., Grcar, J. F., and Rupley, F. M., "OPPDIF: A FORTRAN Computer Program for Computing Opposed-Flow Diffusion Flames," Sandia National Laboratories, Rept.. SAND96-8243, Albuquerque, NM, 1997.

[26] Siegel, R., and Howell, J. R., *Thermal Radiation Heat Transfer*, 4th ed., Taylor & Francis, New York, 2002.

[27] Grosshandler, W., "A Narrow Band Model for Radiation Calculations in a Combustion Environment," National Institute of Standards and Technology, TN 1402, Gaithersburg, MD, 1993.

[28] Lindstedt, P. R., "Soot Formation in Combustion," Springer–Verlag, Berlin, 1994, p. 417.

[29] Puri, R., Richardson, T. F., and Santoro, R. J., "Aerosol Dynamic Processes of Soot Aggregates in a Laminar Ethane Diffusion Flame," *Combustion and Flame*, Vol. 92, No. 3, 1993, pp. 320–333. doi:10.1016/0010-2180(93)90043-3

[30] Frenklach, M., Clary, D. W., Gardier, J., and Stein, S. E., "Detailed Kinetic Modeling of Soot Formation in Shock-Tube Pyrolysis of Acetylene," *20th Symposium (International) on Combustion*, Combustion Institute, Pittsburgh, PA, 1984, pp. 887–901.

[31] Lee, K. B., Thring, M. W., and Beer, J. M., "On the Rate of Combustion of Soot in a Laminar Soot Flame," *Combustion and Flame*, Vol. 6, 1962, pp. 137–145. doi:10.1016/0010-2180(62)90082-2

[32] Schlichting, H., *Boundary Layer Theory*, 7th ed., McGraw—Hill, New York, 1979.

[33] Emmons, H., "The Film Combustion of Liquid Fuel," *Zeitschrift fur Angewandte Mathematik und Mechanik*, Vol. 36, 1956, pp. 60–71. doi:10.1002/zamm.19560360105

[34] Andreussi, P., "Modelling of Laminar Diffusion Flames over a Horizontal Plate," *Combustion and Flame*, Vol. 45, 1982, pp. 1–6. doi:10.1016/0010-2180(82)90027-X

[35] Fujita, O., Ito, K., Ito, H., and Takeshita, Y., "Effect of Thermophoretic Force on Soot Agglomeration Process in Diffusion Flame Under Microgravity," *4th NASA International Microgravity Combustion Workshop*, 1997, pp. 217–222.

T. Jackson
Associate Editor